Initial Characterization of Dark-Field CT on a Clinical Gantry

Manuel Viermetz, Nikolai Gustschin, Clemens Schmid, Jakob Haeusele, Bernhard Gleich, Bernhard Renger, Thomas Koehler, and Franz Pfeiffer

***Abstract*— X-ray computed tomography (CT) is an important non-destructive imaging technique, particularly in clinical diagnostics. Even with the latest innovations like dual-energy and photon-counting CT, the image contrast is solely generated from attenuation in the tissue. An extension – fully compatible with these novelties – is dark-field CT, which retrieves an additional, so-called dark-field contrast. Unlike the attenuation channel, the dark-field channel is sensitive to tissue microstructure and porosity below the resolution of the imaging system, which allows additional insights into the health of the lung tissue or the structure of calcifications. The potential clinical value has been demonstrated in several preclinical studies and recently also in radiography patient studies. Just recently the first dark-field CT for the human body was established at the Technical University of Munich and in this paper, we discuss the performance of this prototype. We evaluate the interferometer components and the imposed challenges that the integration into the CT gantry brings by comparing the results to simulations and measurements at a laboratory setup. The influence of the clinical X-ray source on the Talbot-Lau interferometer and the impact of vibrations, which are immanent on the clinical CT gantry, are analyzed in detail to reveal their characteristic frequencies and origin. A beam hardening correction is introduced as an important step to adapt to the poly-chromatic spectrum and make quantitative dark-field imaging possible. We close with an analysis of the image resolution and the applied patient dose, and conclude that the performance is sufficient to suggest initial patient studies using the presented dark-field CT system.**

***Index Terms*— Computed tomography, dark-field contrast, Talbot-Lau interferometer, X-ray imaging.**

Manuscript received 15 September 2022; revised 9 November 2022; accepted 13 November 2022. Date of publication 17 November 2022; date of current version 3 April 2023. This work was supported in part by the Karlsruhe Nano Micro Facility (KNMF, www.kit.edu/knmf), a Helmholtz Research Infrastructure, Karlsruhe Institute of Technology (KIT); in part by the TUM Institute for Advanced Study; in part by the European Research Council (ERC H2020), under Grant AdG 695045; and in part by the Philips DACH GmbH. *(Corresponding author: Manuel Viermetz.)*

Manuel Viermetz, Nikolai Gustschin, Clemens Schmid, and Jakob Haeusele are with the Chair of Biomedical Physics, School of Natural Sciences, and Munich Institute of Biomedical Engineering, Technical University of Munich, 85748 Garching, Germany (e-mail: manuel.viermetz@tum.de; nikolai.gustschin@tum.de; clemens.schmid@tum.de; jakob.haeusele@tum.de).

Bernhard Gleich is with the Munich Institute of Biomedical Engineering, Technical University of Munich, 85748 Garching, Germany (e-mail: gleich@tum.de).

Bernhard Renger is with the Department of Diagnostic and Interventional Radiology, School of Medicine and Klinikum rechts der Isar, Technical University of Munich, 81675 Munich, Germany (e-mail: renger@tum.de).

Thomas Koehler is with the Philips Research, 22335 Hamburg, Germany, and also with the Institute for Advanced Study, Technical University of Munich, 85748 Garching, Germany (e-mail: thomas.koehler@philips.com).

Franz Pfeiffer is with the Department of Diagnostic and Interventional Radiology and Klinikum rechts der Isar, Technical University of Munich, 81675 Munich, Germany, and also with the Chair of Biomedical Physics, School of Natural Sciences, Institute for Advanced Study, and Munich Institute of Biomedical Engineering, Technical University of Munich, 85748 Garching, Germany (e-mail: franz.pfeiffer@tum.de).

Digital Object Identifier 10.1109/TMI.2022.3222839

I. Introduction

X-RAY imaging is based on the transmittance of the sample material and has become one of the most important non-destructive analysis methods, particularly in medical imaging. Even though innovations like dual-energy and photon-counting CT were introduced recently to clinics, the contrast in CT is still only retrieved from attenuation differences of X-ray photons in the sample. These currently available systems cannot measure the diffraction and small-angle scattering of the transmitted X-rays. However, numerous preclinical studies demonstrated that in particular small-angle scattering, leading to dark-field contrast, can improve medical diagnostics as it reveals tissue microstructure and porosity which lies below the spatial resolution of the system [1], [2], [3], [4]. Therefore, we want to bring Talbot-Lau interferometry to clinical CT, as it allows for simultaneous acquisition and reconstruction of the linear attenuation and linear diffusion coefficient (also called dark-field extinction coefficient) in the sample. In the dark-field channel, small-angle scattering in sub-resolution structures is measured as a signal increase [5], [6] and can then be correlated to the size and shape of the scattering structures without being able to resolve those directly [7], [8], [9], [10].

We recently presented the first dark-field CT system which is based on a clinical CT and allows imaging of the human chest [11]. It is realized by integrating a Talbot-Lau interferometer into the system, i.e., extending the conventional CT gantry by a set of three gratings, which are X-ray absorbing or phase-shifting line patterns with grating periods of a few micrometers. In laboratory systems, such Talbot-Lau interferometers are well established [12], [13], [14], [15], [16], but for the translation to clinical practice several challenges, such as stability and field of view, have to be overcome.

Previous projects by [17] or more recently by [18] made clear that stability of the design is of utmost importance for a successful implementation.

In [19], we discussed the fundamental design criteria of our prototype, including details on the geometric and grating parameters. The first results from the implementation and initial description have been published in [11]. There, we demonstrate that it is feasible to overcome the challenges concerning stability against vibrations, accurate alignment over a large area, and the fabrication of large and hard X-ray compatible gratings.

In this paper, we present a detailed analysis and characterization of the dark-field CT prototype, which has been designed in [19] and was initially presented in [11]. Our focus lies particularly on the experienced vibrations, the interferometer performance, the radiation dose, and the 3D-imaging performance. Other aspects which are evaluated are the performance of the first ever implementation of a triangular G_1 in a dark-field CT setup, the accuracy of the large bent gratings with bending radii ranging between 100 mm and 1000 mm, and the extreme performance dependence on the X-ray source size. Most of the characterization is done by comparing the interferometer which has been implemented into a CT gantry (Brilliance iCT, Royal Philips, The Netherlands) to its implementation at a laboratory setup. The latter implementation is considered as an ideal reference environment which allows us to differentiate between the intrinsic performance of the interferometer and the impact of CT gantry specific influences such as vibrations and the clinical hardware like the X-ray source or detector.

II. Interferometer Principle and Geometry

In the presented dark-field CT prototype, a three grating Talbot-Lau interferometer [20], [21] is designed to fit into the available space on the gantry of a CT system, as illustrated in Fig. 1. It is in an inverse geometry where two X-ray compatible optical gratings, referred to as G_0 and G_1, are positioned close to the X-ray source in front of the patient and the third grating (G_2) is placed on the other side of the bore in front of the detector [22]. As discussed in [19], this geometry is advantageous for implementation into a clinical CT gantry because only relatively small gratings G_0 and G_1 are required and the available space close to the source is efficiently used.

The working principle of Talbot-Lau interferometers is based on G_1 inducing a fine line pattern onto the radiation, which then is attenuated, distorted, and scattered by the attenuation, refraction, and small-angle scattering properties of the sample, respectively [23], [24]. As this fine line pattern cannot be directly resolved by a conventional detector, an analyzer grating G_2 is used, which has the same period as the line pattern, to generate easily resolvable Moiré fringes [24], [25]. To ensure that this conversion utilizing the Moiré effect works also with the extended X-ray source spot, a source grating G_0 must be implemented [20], [21].

The precise setup geometry and grating specifications are derived and listed in [19]. There we decide on a design where the finest grating has a period of only 4.34 μm (G_1) and the coarsest is 45 μm (G_2). Such fine structures are required to be able to resolve the refraction and small-angle scattering of the X-rays in the sample, as these effects are relatively weak at the high X-ray energies compared to, e.g., visible light. The drawback of using such fine grating structures is a high sensitivity to displacement of the gratings during the exposure, which can strongly degrade the imaging performance and has been the major concern during the development. For the assessment of those mechanical vibrations, a vibration sensor (Model 356A17, PCB Piezotronics, New York, USA) is used throughout this study.

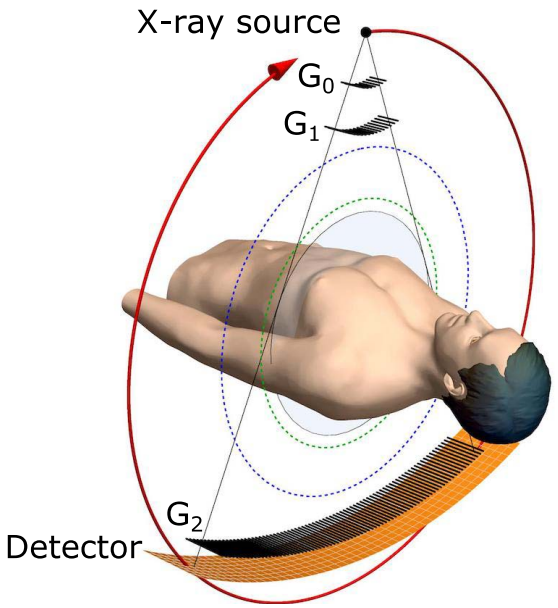

Fig. 1. Cylindrical dark-field CT design with an inverse Talbot-Lau interferometer consisting of bent gratings. The design has been introduced in [19] and makes the best use of the available space in a clinical CT gantry, maintaining the original bore diameter of 70 cm. The field of view is the highlighted area with a diameter of 45 cm, which is only 10% smaller than the original field of view shown in green. The large G_2 is about 80 cm wide and is the only grating in the setup which must be combined from smaller tiles.

III. Performance Evaluation – Laboratory

To evaluate the performance of the interferometer without any vibration-induced artifacts, we install the interferometer in the proposed geometry at a laboratory setup on an optical table for reference measurements. Here, the same grating mounts which have been designed for bending and stable positioning in the CT gantry are used, but the field of view is limited to three G_2 tiles by the setup geometry.

A micro-focus X-ray tube (XWT-160-SE, X-ray Worx, Germany) with a tungsten reflection target is operated at 80 kVp and a filtration is used to match the emitted spectrum to the clinical CT spectrum. A flat-panel detector (XRD 4343, Varex, Utah, USA) acquires the image data and a motorized stage allows re-positioning of G_2 to measure stepping curves. As proposed in [25] a stepping acquisition is a set of projections where one grating is moved perpendicular to the grating lines in multiple steps over one period.

In Fig. 2a an example projection is shown where the characteristic fringe pattern and two small gaps between the three G_2 tiles are visible. The intensity measurements of one pixel at 31 stepping positions is plotted in Fig. 2b representing

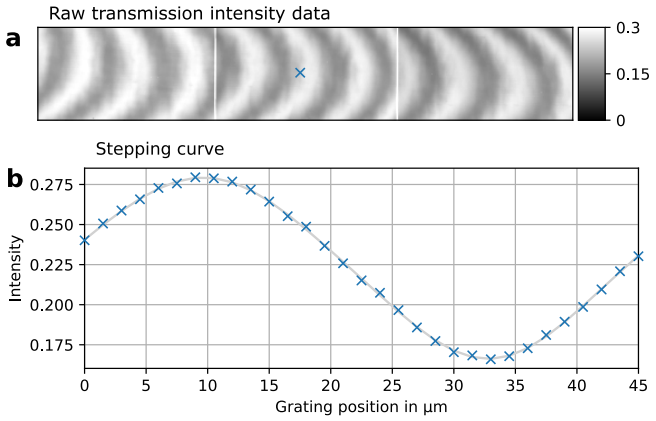

Fig. 2. Experimental data measured at laboratory setup. **a**, Limited by the setup geometry, the field of view shows only three G_2 tiles. The interferometer is adjusted to have equidistant vertical fringes which are continuous over the tile borders. Gaps between the tiles are visible as white lines. **b**, An example of a stepping curve acquired with a motorized stage using 31 steps over one G_2 period. No higher order contributions are visible, i.e., no deviations from the sinusoidal curve in gray. The system's visibility is calculated from the amplitude and mean of the curve.

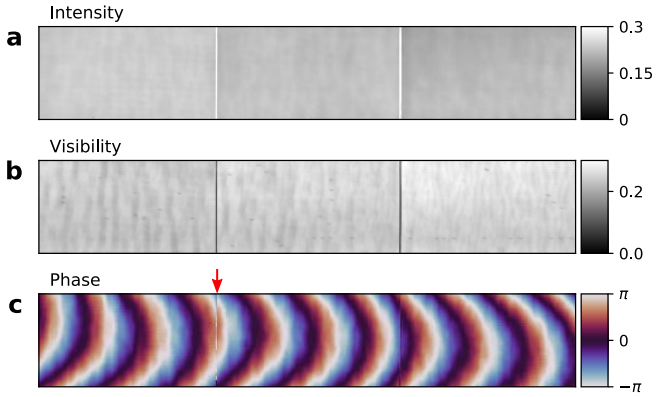

Fig. 3. Interferometer performance at a laboratory implementation for reference. **a**, After processing the stepping data, a homogeneous intensity transmitted through the interferometer of 23% demonstrates that cylindrical bending minimizes shadowing. **b**, The mean visibility of the reference implementation is 0.24. It is reduced by small dot-like artifacts originating from defects and some diffuse vertical lines from inclination errors in G_0 and G_1. **c**, The phase can be adjusted to be continuous between G_2 tiles, as demonstrated at the right inter-grating gap. At the left gap, the process was stopped early, showing a local jump in interferometer phase (see red arrow).

a stepping curve y_t, where the index t corresponds to the step-number. A sinusoidal curve expressed by

$$y_t = I \cdot (1 + V \cdot \sin(\phi + \Phi_t)) , \tag{1}$$

is then fitted to each pixel's measurements, yielding an intensity I, visibility V, and phase ϕ for each pixel, while Φ_t are the known stepping phase positions which are the same for all pixels at each step t [7], [26]. These three quantities, i.e., intensity, visibility, and interferometer phase, are the important performance measures in Talbot-Lau interferometry and their analysis allows us to reveal potential problems in the imaging system and its components. The field of view of the laboratory implementation is limited by the opening angle of the X-ray tube and the detector size to three G_2 tiles. Nevertheless, this is sufficient for general performance evaluation and reference measurements, which afterwards are compared with results from the gantry implementation. Only for some aspects, e.g., shadowing artifacts, the laboratory dimensions are too small and this must be evaluated directly in the gantry implementation.

The data model in (1) represents only the first order of the Moiré fringe pattern, which is used in most processing approaches for Talbot-Lau interferometry. In our recent simulation-based study we, however, found that for an interferometer with a triangular G_1 some higher order terms can gain importance and might become visible in the Moiré pattern and the stepping curve [19]. The study also reports that the higher order contributions decrease when a G_0 is implemented.

As can be seen in the stepping curve plotted in Fig. 2b, we find no higher order contributions in the experimental data acquired even at our laboratory setup implementation and the stepping curve clearly follows the sinusoidal curve (gray line). We conclude that as our setup uses a G_0 the higher orders are blurred and lie below the noise level.

After decomposition of the stepping data into the three image channels, the intensity results, shown in Fig. 3a, allow an assessment of the interferometer transmittance, i.e., how much input flux is lost in the gratings. The mean transmission is about 23% which lies within the expectations for the setup as it consists of two absorption gratings G_0 and G_2, and their attenuation is dominated by the respective duty-cycles of 0.6±0.02 and 0.56±0.02 which by design stop 60% and 56% of the X-ray flux. Fabrication variations or defects in, e.g., the height or the duty-cycle of the grating structures, or impurities in the substrate can lead to variations of the interferometer's transmittance, but here no problems are found. Absorption in the grating substrate can be neglected because the optimized substrate materials (graphite and polyimide) lead to only about 1% total intensity loss [27].

In the visibility result, shown in Fig. 3b, small dot-like defects are visible which come from droplet-like electroplating faults during fabrication of G_1. Besides some diffuse vertical lines, which are related to slightly distorted or inclined lamella in G_0 which lead to local shadowing artifacts [28] no further degradation is found in the visibility or intensity channel. This is an important finding, particularly as this demonstrates that bending gratings to focus onto the X-ray source spot does not degrade them. The mean visibility of the evaluated area in this reference implementation is 0.24 and almost constant over the entire field of view.

The processing result in Fig. 3c shows the phase of the interferometer, which is continuous between the two right-most G_2 tiles. To demonstrate the possible alignment error, the alignment process of the left G_2 tile was not finished, resulting in a discontinuity of the interferometer phase at the edge. It is important to be able to adjust each G_2 tile to the correct phase in order to minimize stitching artifacts and unusable pixel columns in the CT gantry implementation [29], [30].

IV. Translation From Laboratory to Gantry

A specialized mount has been developed to mount G_0 and G_1 together as a single unit on the CT gantry. It ensures consistent alignment between the two first gratings, precise

bending, and avoids complicated adjustment inside the gantry. Once this assembly is installed into the collimator box of the CT, it is difficult to access. In the collimator box the G_0 and G_1 unit replaces one of the bow-tie filters, and leaves all other components, e.g., the motorized collimator blades in their original state. This is important as it allows collimating the X-ray beam to a specific number of detector rows and thus is mandatory to minimize patient dose. After the integration of G_0 and G_1 into the system, the thirteen G_2 grating tiles are installed and adjusted relative to the G_0 and G_1 assembly. In this step, the Moiré fringe pattern is optimized to have 0.1 fringes per mm, as this is optimal for data processing and the reconstruction pipeline.

During operation, the gantry rotates with a rotation time ranging from 0.27 s to 1.5 s and acquires 2400 projections over 2π of an axial tomography scan. In the presented prototype dark-field CT, 32 detector lines are used, resulting in a coverage of 20 mm in the iso-center. To extend this coverage, either multiple axial scans can be stacked or a helical acquisition is possible. In contrast to the laboratory implementation in Sec. III, the presented dark-field CT has no stepping actuator and relies on system intrinsic vibrations. These lead to a small displacement of the gratings between each projection measurement, consequently a sequence of projections can be interpreted as an irregularly sampled stepping curve. Active stepping therefore becomes obsolete at the cost of irregular stepping positions and less influence on the width between the steps. To still be able to draw all information from this data, a specialized processing pipeline has been developed which can separate the three image channels, i.e., intensity, visibility, and interferometer phase. It was initially sketched in [11] and a full description of the processing framework including all the related optimization and correction mechanisms is presented in [31]. With this processing applied to the measured data, we can extract the interferometer state at each projection. This allows us to evaluate the fluctuations in the various image channels with a high temporal resolution.

V. Performance Evaluation – Clinical Gantry

A. Transmission Analysis

Shadowing artifacts in the high aspect ratio gratings can be reduced by bending the gratings cylindrically to focus the lamella towards the X-ray source spot [32]. While the limited field of view in the laboratory implementation did not allow a full analysis of this approach, a transmission performance analysis of the entire gratings G_0 and G_2 is possible in the final CT implementation and is shown in Fig. 4.

The results for the G_0 transmission in Fig. 4a reveal that transmission is highest in the center and reduces to left and right. Several reasons can lead to this behavior and are difficult to differentiate. Via angular X-ray transmission analysis [28], we found that the used G_0 has imperfections towards the left and right edges, which result in a reduction of transmission also in the bent state. Another aspect which must be considered is the shadowing inside the grating structure caused by the extended X-ray source spot. We refer to this effect as the *acceptance* of the grating, which depends on the aspect ratio

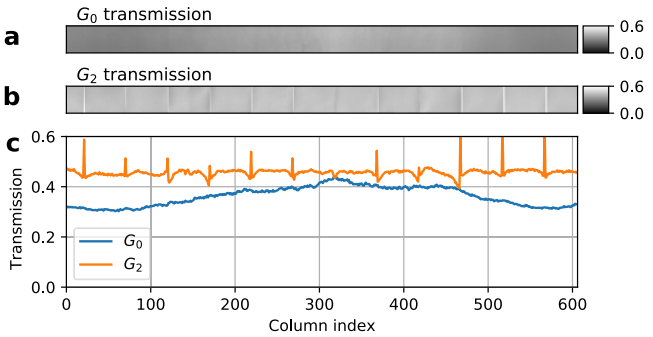

Fig. 4. Transmission analysis of the bent gratings G_0 and G_2 in the CT gantry without gantry rotation. **a**, The G_0 has a mean transmission of 40% which is expected for its grating parameters. Due to grating imperfections and the acceptance effect (i.e., from the high aspect ratio and large source spot size) the outermost regions on the left and right have reduced transmission. No defects related to the small bending radius of 100 mm are found. **b**, Analysis of the G_2 tiles transmission shows only local variations and tile-wise differences which will be corrected during reconstruction. The mean transmission is around 45%, which is expected for a grating with duty-cycle of around 56% with a negligible bridge-fraction of only 1%. **c**, Line plot of the central detector row from a and b. Here, strong transmission peaks occur at the G_2 tile-gaps and for G_0 a decay to the left and right is observed.

and the source size. At clinical CT X-ray sources, the inclined anode surface leads to variable source width [33]. It is smallest for the central beam through the iso-center and increases for larger fan angles towards the outer detector columns. Since the aspect ratio of the grating is constant, the acceptance of G_0 decreases for larger fan angles and consequently transmission and visibility are reduced in these areas. As a consequence, only in the center, for which the X-ray source spot is smallest, the expected transmission value of 45% is met and otherwise the grating's acceptance leads to a slight intensity decrease towards the left and right. Nevertheless, we conclude that bending of the G_0 minimizes the amount of shadowing to a tolerable level. As G_0 has a bending radius of only 100 mm, this demonstrates that, except for some acceptance-related residual shadowing, bending can be applied at relatively small radii. In our dark-field CT prototype this allows us to implement an interferometer with a fan opening of about 47° which is currently not feasible with any other shadowing suppression method.

In contrast to the G_0 results, G_2 has an almost optimal transmittance, as only small transmission fluctuations are visible in Fig. 4b. They are caused by imperfections from the fabrication process and are always localized to a single G_2 tile.

The measured transmission values lie around 45% which matches our expectations for the G_2 design. This shows that this grating works as intended over the entire field of view, and no shadowing is found. This is important because any additional and undesired absorption caused by G_2, i.e., shadowing or defects in G_2, would result in an even higher dose penalty than G_2 causes by design as it is positioned behind the patient. This result demonstrates that cylindrical bending also works well for larger bending radii, i.e., here 1000 mm, and gratings which are combined from several smaller, individually bent, tiles.

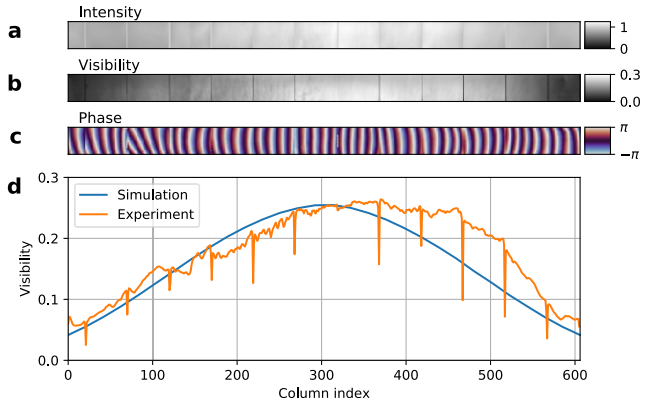

Fig. 5. Dark-field CT performance in rotating gantry. **a**, Intensity is rather homogeneous with a shallow maximum in the center due to the G_0 acceptance. This pattern is similar to the effect of the bow-tie filter regularly used in conventional CT. Thus, this distribution has no negative impact. **b**, Interferometer visibility is highest in the center, exceeding 0.25. The mean visibility of the central 50% of the field of view is 0.22 and the mean visibility of the whole field of view is 0.18. No significant defects related to grating fabrication are found. **c**, A Moiré pattern with a horizontal fringe period of around 10 pixels, is visible in the phase image. **d**, A line plot of the system's visibility shows the dependency of the visibility on the fan angle, i.e., detector column. The visibility drop is related to the limited acceptance of the high aspect-ratio G_0. The experimental results match reasonably well to simulations taking the limited acceptance into account. Deviations from the simulation can be explained by the strong impact of duty-cycle variations and geometry mismatch.

The results also show that cylindrical bending is sufficient because no vertical transmission gradients are found. This is expected since shadowing is strongly direction-dependent and when the angle of incidence is parallel to the grating lines, the performance of the interferometer will not be reduced and no shadowing occurs [32]. For G_1 the transmission analysis is skipped as shadowing is no issue for its comparably small virtual aspect ratio of only 8. Furthermore, it is designed as a phase-grating with a transmittance of about 90%. Consequently, it has only a small impact on the X-ray flux, compared to G_0 and G_2. Potential defects in the grating structure would not lead to any significant changes in the transmission, and can more easily be revealed by evaluating the interferometer visibility.

B. Interferometer Performance Analysis

To evaluate the interferometer performance of the dark-field CT prototype, a standard axial scan with 1 s rotation time without any sample is measured. The acquired 2400 projections at random stepping positions are then processed, and we obtain the performance measures intensity, visibility, and interferometer phase as shown in Fig. 5.

As expected from the previously discussed transmission analysis, the processed system intensity is relatively flat, with a wide maximum in the center which is caused by the acceptance of the G_0. The apparent intensity variation is similar to the effects of a bow-tie filter in conventional CT, where it is used to reduce patient dose and achieve a more homogeneous noise level across the image. Therefore, the intensity gradient is actually advantageous for CT imaging, and we can for now omit the use of a bow-tie filter. To further optimize the intensity variation with the fan angle, the implementation of a specifically shaped bow-tie filter can easily be added to the G_0 and G_1 assembly.

The system visibility is shown in Fig. 5b and an evaluation of the three central tiles yields a mean visibility of 0.24. The same three tiles have previously been evaluated in the laboratory setup, and comparing this value to the findings in Section III shows that a comparable interferometer visibility can be achieved in the clinical CT gantry as in the laboratory setup. It is important to highlight that this only represents the central region of the CT's field of view, and we clearly see a reduction of visibility towards the left and right edges. These areas had been inaccessible in the laboratory implementation due to the limited field of view.

Quality variations in G_0 and G_1 can result in such a visibility gradient towards the edges, and also the acceptance of the G_0 leads to a reduction of the visibility. The latter effect reduces the quality of the slit-sources, created by G_0, in the outer regions of the interferometer, i.e., where the fan angles are large. This relation has recently been evaluated in detail in [19] Section VI. When the source spot is significantly large, i.e., if it is seen under large fan angles, an increasing fraction of radiation which transverses the grating leaks through the absorbing structures. This leaked radiation subsequently creates an incoherent intensity offset, which lowers the system visibility. In the visibility line plot, shown in Fig. 5, the experimental results are overlaid with simulation results considering the G_0 acceptance. Remaining differences probably arise from quality and geometry deviations between the simulation and the setup, but the general trend matches. It must be noted that in our previous work on the design considerations for this dark-field CT [19], we identified that the tolerances for the grating periods have to be tightly met and otherwise visibility degradation for outer fan angles can occur. By thorough inspection and characterization of the fabricated gratings, we were able to ensure that this effect was kept to a minimum and only the visibility is primarily degraded by the G_0 acceptance.

Between adjacent G_2 tiles, there are one pixel wide columns with reduced visibility (sharp drops in Fig. 5d) because there remain small gaps between the tiles. Nevertheless, there are no columns where the visibility drops to zero and the density of the fringe pattern is relatively constant and mostly almost continuous over the tile borders. While the orientation of the fringe pattern is not an essential requirement, its periodicity should be in the order of one fringe per eight pixels to be optimal for the reconstruction [34].

VI. Vibration Analysis

As noted in Section IV, the system-intrinsic vibrations are utilized for random phase stepping. Usually, the aim is to avoid any kind of vibrations in interferometry setups, but total decoupling is not feasible on a CT gantry. Some mandatory components of a clinical CT consist of mechanical parts which continuously induce vibrations. Sources of vibrations on the CT gantry are the pump of the cooling unit and the rotating anode of the X-ray source. Naturally, these components could be optimized for fewer vibrations. However, it would have gone beyond the scope of our objective of upgrading a

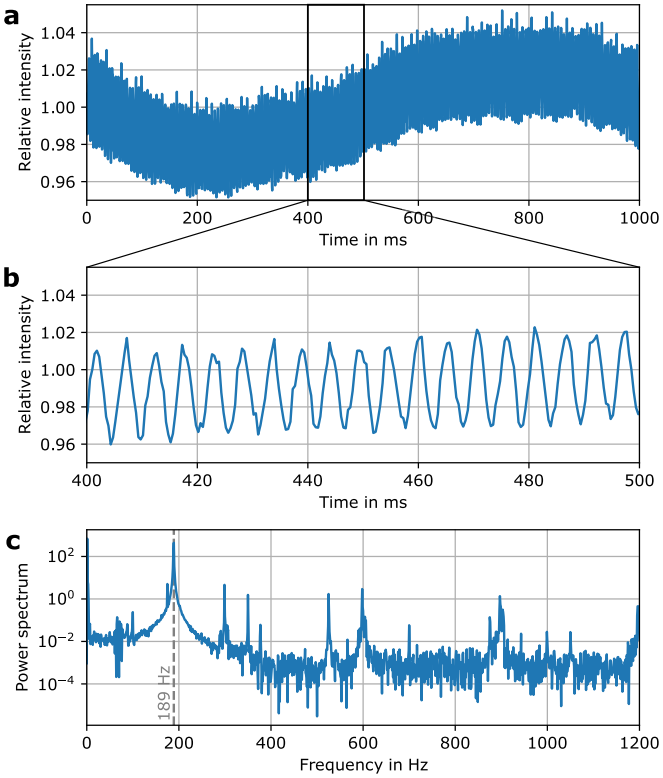

Fig. 6. Variation in the intensity channel during a scan. **a**, In the 2400 projections measured during one rotation, the intensity varies with a low frequency related to the gantry rotation overlaid with a high frequency. **b**, Clipped section from a. The oscillation is dominated by one frequency, which is stable over the whole scan time. **c**, Fourier analysis of the coefficient yields that besides the low frequency (1 Hz) the dominant frequency is at 189 Hz.

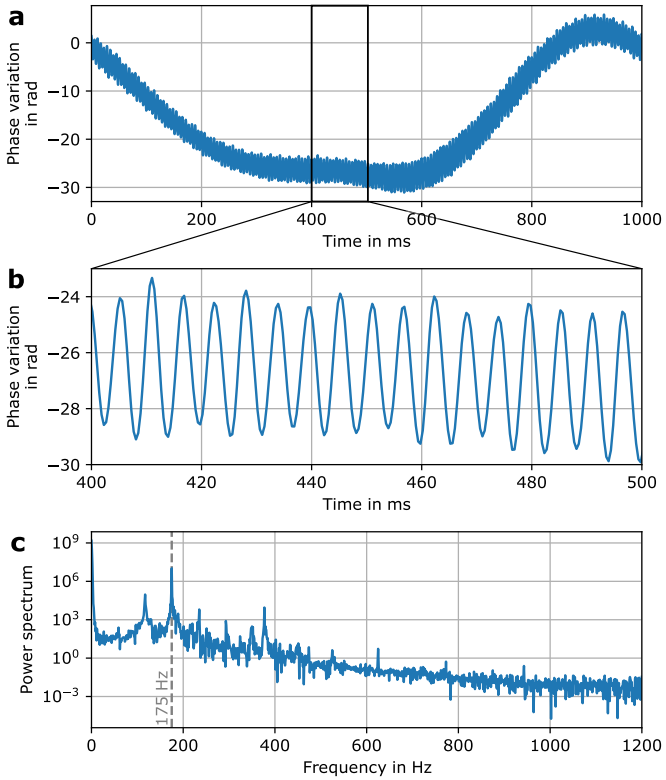

Fig. 7. Variation of the interferometer phase during a scan. **a**, During one rotation the interferometer phase varies over several π with a low frequency. **b**, Clipped section from a. The oscillation is of sinusoidal nature and continuous over the whole scan time. **c**, Fourier analysis of the coefficient yields that besides the low frequency, the dominant high frequency is at 175 Hz.

conventional CT to a dark-field CT. Finally, the gantry itself is not perfectly in balance during its rotation and introduces vibration, yet at relatively low frequencies of the rotation period which is between 1.5 s and 0.27 s. As this particular product line comes with an air bearing [35], which lets the gantry float on an air cushion, an effective decoupling of the stator and the surrounding is ensured.

The various sources of vibration lead to displacement of the gratings, and this consequently gives rise to fluctuation of the interferometer state. The processing of the air-scan data models and fits these fluctuations and returns the interferometer performance parameters and all repetitive deviations [31]. These processing results therefore contain information about the vibrations and how they alter the intensity, visibility, and phase of the Moiré pattern.

Figures 6, 7, and 8 show examples of the fluctuations in the intensity, visibility, and phase channels, respectively, during a scan without a sample with 1.0 s rotation period. These curves were extracted during the data processing and the plots allow us to identify the different sources of fluctuations by frequency analysis.

Fig. 6 shows the analysis of the intensity fluctuations, and we find two dominant oscillation frequencies in these plots: a low frequency oscillation at 1 Hz and a high frequency at 189 Hz. The Fourier analysis also shows other frequency contributions, but these are at least two orders of magnitude less intense. The origin of the low frequency oscillation clearly is the gantry rotation, and it is consistent in amplitude and phase between multiple scans. The source of the high frequency variation has been identified as the X-ray tube driver, which impels the anode. This asynchronous motor is operated at a frequency of 189 Hz and induces the observed intensity fluctuations through electromagnetic interference. We assume that the variations might be caused by electromagnetic distortion of the X-ray source spot shape and hence has influence on the total X-ray flux. As we can see in Fig. 6 the total amplitude of the intensity variations is only in the order of $\pm 4\%$ which is in conventional CT corrected by a reference detector, but due to space restrictions this device has been removed and thus our processing must correct for it.

In Fig. 7 the characteristic vibration properties in the interferometer phase reveal an oscillation at 175 Hz which is again overlaid with the 1 Hz from the gantry rotation. During the rotation, the changing gravity together with the centrifugal forces lead to slight deformations of the gantry and the grating mounts. The interferometer is highly sensitive to such displacements in the micrometer range by change of the interferometer phase. The high frequency component here is induced by the rotation frequency of the X-ray tube anode, which is driven by the previously discussed asynchronous motor. It is characteristic for an asynchronous motor that there is a small slippage between the rotating magnetic field excited by the stator coils and the actual rotation of the rotor, i.e., the anode. Consequently, the anode rotates at a

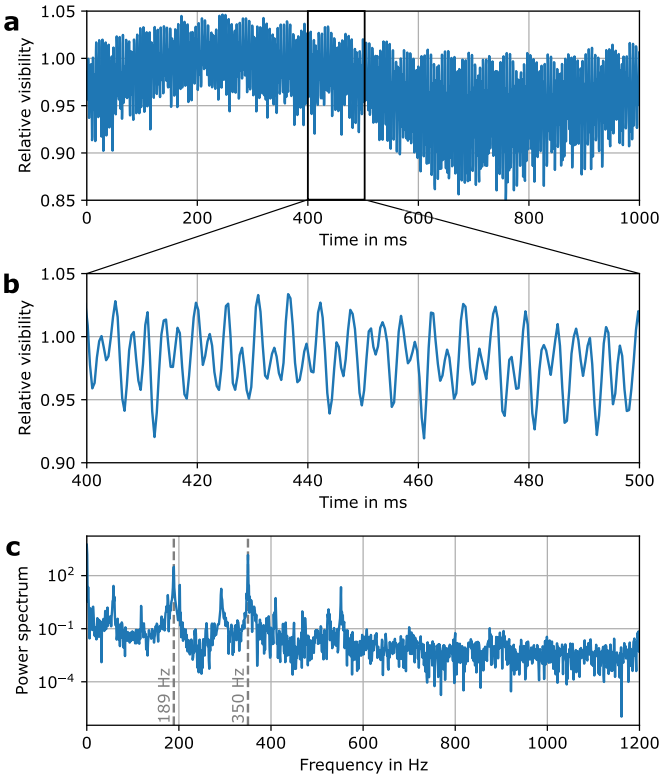

Fig. 8. Variation of the system visibility during a scan. **a**, In the 2400 projections measured during one rotation, the visibility varies moderately with a low frequency related to the gantry rotation overlaid with a high frequency. **b**, Clipped section from a. This oscillation is a combination of two almost equally intense frequencies, which leads to a beat pattern. **c**, Fourier analysis of the coefficient yields that besides the 1 Hz frequency, the high frequencies 189 Hz and 350 Hz are most dominant.

slightly lower frequency than the 189 Hz of the driver [33]. For verification, we attached a vibration sensor to the X-ray tube housing and analyzed the spin-up phase of the anode, which stabilized at 175 Hz. This mechanical oscillation from the anode rotation presumably displaces the gratings, which leads to the high-frequency phase change of the interferometer visible in Fig. 7b. Since this displacement is only in the range of a few micrometers it is too small to induce any shadowing artifacts, consequently, we see no influence of this mechanical oscillation in the intensity channel.

It is important to point out that any movement of a grating during the measurement leads to a reduced visibility due to the smearing of the fringe pattern [17]. We therefore expect a visibility variation at twice the frequency of the previously evaluated interferometer phase variation (175 Hz) coupled to the absolute speed of the gratings, i.e., the absolute rate of phase change. The derivation of the exact relation can be found in [31, Eq. 7]. In Fig. 8 the processing results of the visibility variation shows this effect as there is a peak at 350 Hz in the frequency spectrum. This is twice the mechanical oscillation frequency which is induced by the anode rotation, representing the speed of the gratings during the acquisition of the projection. Since the visibility of the system is independent of the position of the interferometer phase, there is no peak at 175 Hz in the visibility variation. Another dominant frequency in the visibility channel is the 189 Hz oscillation which previously was related to the electromagnetically induced change of X-ray flux, which we already found in the intensity in Fig. 6. This supports our hypothesis that there is an electromagnetic interference between anode motor and interferometer, e.g., by small distortions of the focal spot which can lead to visibility changes if the source size varies. The two frequencies at 189 Hz and 350 Hz have similar strength, consequently, the resulting pattern in Fig. 8b is a rather chaotic beat pattern as the two frequencies interfere.

Besides the two most dominant base frequencies (175 Hz and 189 Hz) identified in the analyses, also other frequencies with lower contributions are present. Particularly, peaks at some multiples of 58 Hz can be found which are related to the pump of the cooling unit and have also been verified with the vibration sensor. However, compared to the impact of the anode drive and the anode rotation frequency, the contribution of other components is small.

This analysis shows that the system is in a perturbed state. However, the underlying characteristics are reproducible because the sources of vibration do not change their characteristics from scan to scan. While for the gantry rotation induced variations the amplitude and phase is reproducible from scan to scan, for the high-frequency oscillations only their amplitude can be considered as consistent between scans. The phase of these high-frequency variations is only stable during a single scan, but not on a scan-to-scan-basis. As for example the visibility variation follows from the speed, i.e., first derivative, of the interferometer phase, there is clearly a link between those two oscillations. Such correlations between the image channels can be utilized during the data processing of sample scan data, where the signal produced by the sample must be separated from the oscillations in the interferometer.

VII. Beam Hardening in Dark-Field CT

One of the most common effects in conventional clinical CT is beam hardening. It is caused by the polychromatic X-ray spectrum and the energy dependent attenuation in the sample [36] and can lead to an underestimation of the sample's attenuation coefficient. Since the visibility of the Talbot-Lau interferometer is also energy-dependent, there is a similar effect which can create an artificial dark-field signal even when no small-angle scattering happened [37]. Additionally, analogous to attenuation imaging, there is also an energy dependency of the small-angle scattering in the sample [8], [10] and the effect of visibility hardening, as described in [38]. Most dominant in our prototype system, however, is the beam hardening effects caused by energy-dependent performance of the interferometer components (i.e., the absorption gratings G_0 and G_2 performance underlying the attenuation coefficient) which is corrected by the following approach.

In the attenuation channel, beam hardening leads to an underestimation of the sample's attenuation coefficient. Contrary, in the dark-field channel it can lead to an overestimation of the linear diffusion coefficient, i.e., a signal which is not caused by small-angle scattering. This behavior can be seen in the tomographic reconstruction in Fig. 9a where a phantom consisting of a polyoxymethylene (POM) cylinder in the center and a surrounding ring of neoprene

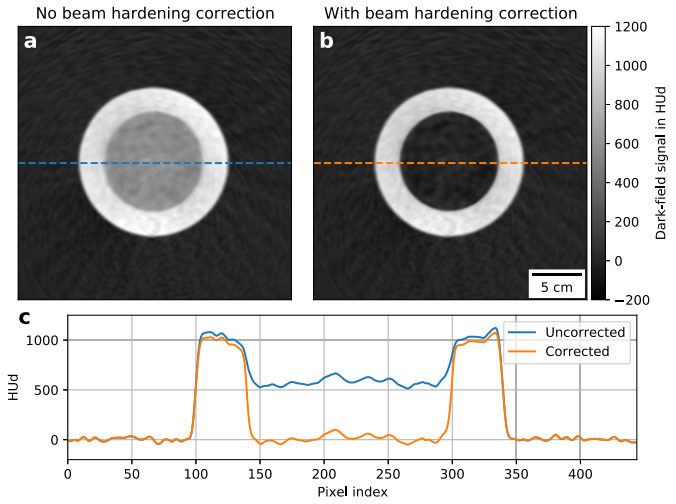

Fig. 9. Dark-field signal reconstruction before and after beam hardening correction. The phantom consists of two materials; a POM cylinder which only attenuates and a neoprene ring which also generates a dark-field signal. **a**, Without any beam hardening correction, a strong dark-field signal is reconstructed for the POM cylinder. **b**, After applying the correction, the POM cylinder has no dark-field signal and only the signal of the neoprene ring remains. **c**, The line plot through the reconstruction images demonstrates how the POM cylinder signal is corrected.

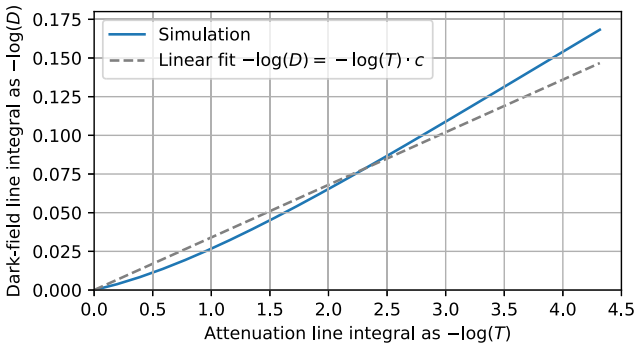

Fig. 10. Simulation results of beam hardening induced relative visibility reduction, which would lead to a reconstruction of an artificial dark-field signal. Filtration from different thicknesses of POM samples are simulated, and the resulting -log of the attenuation signal is plotted against the -log of the relative visibility reduction. The retrieved relative visibility reduction comes from hardening effects and does not represent small-angle scattering in the sample. We apply a correction based on the indicated linear fit to reduce the beam hardening in the tomographic reconstruction.

is shown. While the neoprene has a porous structure which leads to small-angle scattering and thus to a dark-field signal, the homogeneous POM should not have any dark-field signal as it does not generate any small-angle scattering. Contrary, a significant dark-field signal is reconstructed for the POM cylinder, as can also be seen in the line plot in Fig. 9c. We can illustrate this behavior in Fig. 10 where different POM sample thicknesses are used as spectral filters in a simulation of the interferometer performance based on the framework presented in [19]. We find that – while measured intensity varies as expected for the different POM thicknesses – also a relative visibility reduction appears, which is caused by the hardening of the spectrum and not by any small-angle scattering. As an approximation, the relation between measured attenuation and this hardening induced relative visibility reduction can be fitted linearly, which allows us to implement a simple yet effective beam hardening correction.

Our proposed correction is similar to previous work by [37] and [39], but easier to calibrate because it is based on either the aforementioned simulation in Fig. 10 or a calibration scan of a non small-angle scattering object such as water or POM. The measured relative visibility reduction, i.e., $V/V_{\text{ref}} = D_{\text{meas}}$, is a combination of the visibility reduction D_{cor} induced by small-angle scattering and a component $f(T_{\text{meas}})$ from beam hardening which depends on the transmission $I/I_{\text{ref}} = T_{\text{meas}}$ and hence on the attenuation induced by the sample,

$$D_{\text{meas}} = D_{\text{cor}} \cdot f(T_{\text{meas}}). \tag{2}$$

From calibration data as plotted in Fig. 10 and by implying that the examined sample material should not generate any small-angle scattering, i.e., no visibility reduction and consequently $D_{\text{cor}} = 1$, we can find a correction function based on the linear approximation in the log-log-plot,

$$D_{\text{meas}} = \underbrace{D_{\text{cor}}}_{=1} \cdot f(T_{\text{meas}}) = (T_{\text{meas}})^{c}. \tag{3}$$

The calibration factor c can be extracted from a test measurement and is afterwards used to correct sample scans, by applying:

$$D_{\text{cor}} = D_{\text{meas}} \cdot (T_{\text{meas}})^{-c}. \tag{4}$$

In our prototype system, this calibration factor is a global value for all detector pixels and constant for all scans. Only after changes to the grating configuration or the X-ray spectrum, a new calibration is required.

After the beam hardening correction is applied, only the visibility reduction related to small-angle scattering in the material should remain as D_{cor}. Since the method is calibrated to only one soft-tissue equivalent material, strongly attenuating materials such as bones can cause artifacts. It is expected that for those materials, e.g., metal or bone tissue, the hardening effect on the spectrum leads to a stronger overestimation of the dark-field signal and will require the development of a more refined method. For first tomographic reconstructions, however, this single material approach is sufficient because it corrects the overestimation of dark-field signal in soft tissues. There are no beam hardening related artifacts remaining, as can be seen in the reconstruction results in, e.g., Figs. 9, 11, or 12. Consequently, for now, no further beam hardening corrections are applied to the data for our presented dark-field CT scans.

VIII. Resolution

The spatial resolution is a crucial feature of CT in clinical routine, and typically is around 10 lp/cm for state-of-the-art CT scanners in the clinics [40]. At the presented dark-field CT, due to the modifications and the extension of the processing currently some restrictions limit the spatial resolution.

In clinical CT, a flying focal spot alternates between slightly displaced source positions for every projection and is used to increase the spatial resolution of the reconstruction [41]. This feature has been deactivated in the present implementation, and instead a stationary X-ray focal spot is used for maximum stability and to simplify data processing. With an adapted

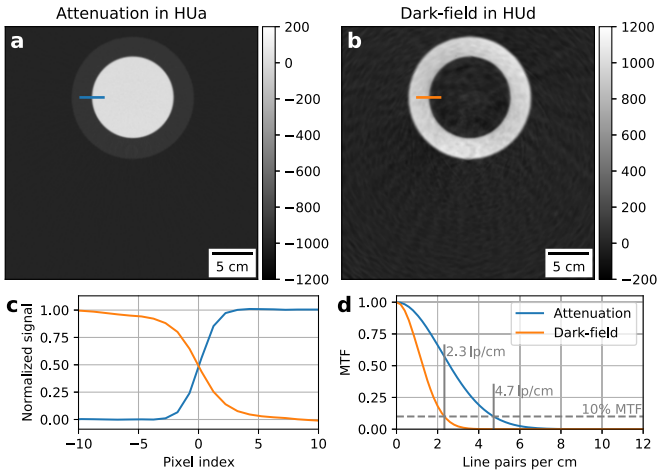

Fig. 11. Attenuation and dark-field reconstruction resolution analysis. The test sample is positioned 6.5 cm above the iso-center. **a** and **b**, Reconstructions of a neoprene and POM cylinder phantom in attenuation and dark-field, respectively. **c**, The edge spread is analyzed at sharp interfaces in the image highlighted by the line plot in a and b. The values are normalized for better visualization. **d**, The modulation transfer function (MTF) in the two modalities shows that attenuation has a resolution of 4.7 lp/cm while the dark-field is less sharply reconstructed with 2.3 lp/cm, both at 10% of the MTF.

processing, i.e., separate for each focal spot position, dark-field CT with flying focal spot should be feasible. However, for now, this simplification comes at the cost of spatial resolution.

A significant resolution loss is expected from the processing, as it is based on sliding-window signal extraction. Here, several consecutive projections are combined to one projection under the assumption that the sample movement is insignificant [42] (i.e., the variation of the intensity within the window is dominated by the change of the relative grating positions and not by the changing line path during the rotation). The ignored movement within a set of projections caused by the system rotation introduces motion artifacts in the transmission and dark-field signal and leads to a blurring of the reconstructed image. At the presented dark-field CT prototype, the window-size is 17 projections for the scans shown throughout this work. Furthermore, a weighted median filter is applied on the dark-field channel in projection-space, which also lowers the spatial resolution [43]. This filter is adaptive to the count rate and helps to avoid artifacts when X-ray flux is low, e.g., in low-dose scans or when strongly attenuating samples are examined, as in these cases the extraction of the dark-field signal otherwise can become biased and unstable [44].

To analyze the effective image resolution of the presented dark-field CT, we use the filtered back-projection reconstruction of the previously introduced POM and neoprene cylinder phantom. The object has been positioned 6.5 cm shifted from the iso-center to include the blurring effect of the sliding window processing. This contribution would vanish if the cylindrical objects were placed in the iso-center because then they would appear stationary in the sinogram and the sliding windows. This scan was measured with 1 s rotation period, 80 kVp, and 300 mA tube current, i.e., at a comparably low radiation dose and a ramp filter is used during the reconstruction. From the sharpness of the interface between POM and neoprene, the edge spread function and subsequently the modulation transfer function (MTF) as a measure for the resolution is extracted. Results are shown in Fig. 11c and d. In the attenuation image the MTF drops to 10% at 4.7 lp/cm and in the dark-field channel the drop is already at 2.3 lp/cm. As expected, the results show that our prototype system has a lower resolution compared to state-of-the-art clinical CT. Reasons for the loss of resolution are the missing flying focal spot, blurring induced by the sliding-window signal extraction which neglects the system rotation, and the use of a weighted median filter in the dark-field channel.

IX. Dose Estimation

For clinical relevance of the presented dark-field CT system, the applied patient dose level must be in a reasonable range. In clinical practice, chest CT protocols have a wide range of applicable computed tomography dose index $CTDI_{vol}$ from 4 mGy up to 10 mGy [45].

To analyze the radiation dose at the presented dark-field CT, the constancy test protocol [46] is used with a standard body phantom of 32 cm diameter and a calibrated Dosimeter (NOMEX, PTW, Germany). We found that the scanner settings 80 kVp and 550 mAs, which have been used for the first published results of a human-sized anthropomorphic body phantom in [11], lead to a $CTDI_{vol}$ of 7.4 mGy.

To demonstrate that dark-field CT scans are feasible well within the suggested dose index range, a scan of the anthropomorphic body phantom and neoprene insert with a $CTDI_{vol}$ of only 4.0 mGy is shown in Fig. 12 (scanned at 80 kVp with 300 mAs). Due to the lower X-ray flux in this scan, a stronger noise reduction via the adaptive filter in the dark-field channel is required and leads to a lower resolution in this channel. Nevertheless, the spatial resolution remains sufficient to easily resolve the individual tubes, and we expect that already with this resolution a diagnostic value is provided by the dark-field signal. However, future work including reader studies with radiologists will be required to answer this research question.

The conducted measurements also confirmed the findings in Section V-A that the G_0 absorbs roughly 50% of the generated X-rays before the patient. This means that a dark-field CT requires twice the mAs of a conventional CT to apply the same $CTDI_{vol}$.

X. Discussion

The presented results demonstrate that dark-field CT of the human body is feasible using a Talbot-Lau interferometer in a state of the art clinical CT gantry. Previous publications discussed the design, processing, and the initial implementation of the dark-field CT system [11], [19], [31]. Here, a detailed characterization of the interferometer analyses the challenges that the translation from optical bench to rotating gantry brings and shows insights into the particular solutions.

We found that the interferometer performs comparable in the clinical CT gantry and in the laboratory implementation, as similar visibility and transmission is achieved in both setups. From this, we can conclude that the translation from laboratory to clinical gantry works and that the presented approaches to solve the related challenges such as shadowing, vibrations, or the focal spot size were successful. Our results demonstrate that the vibrations, the clinical X-ray detector, and the rotation of the gantry have no major impact on the

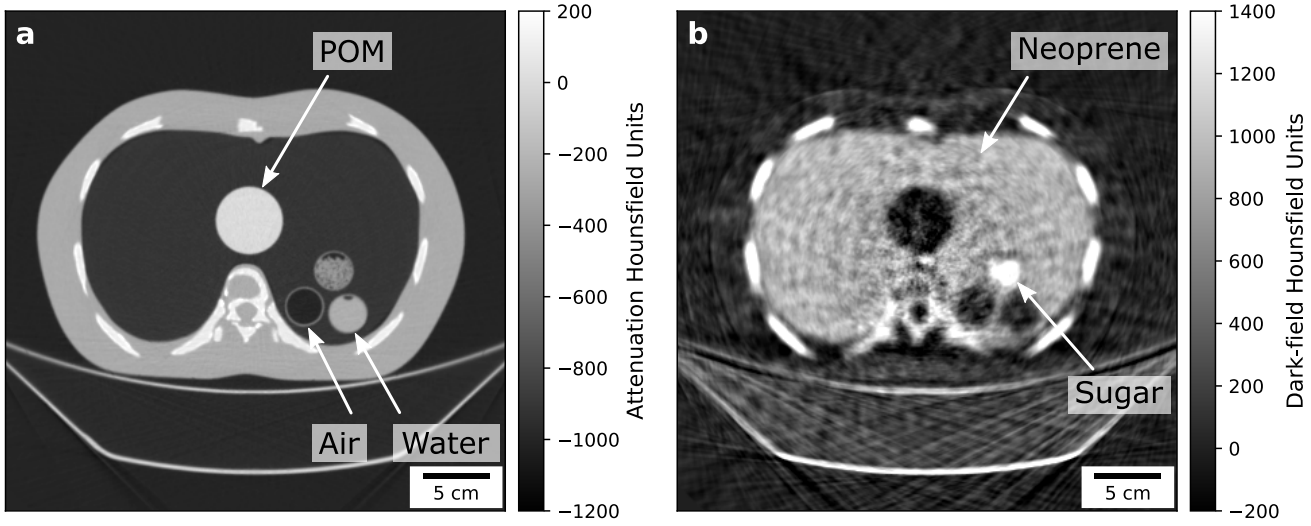

Fig. 12. Attenuation and dark-field reconstruction of human body phantom at a $CTDI_{vol}$ of 4.0 mGy, scanned at 80 kVp with 300 mAs. The anthropomorphic CT phantom is filled with a neoprene insert, which is used to model the lung tissue. The low density and high porosity of the neoprene is similar to the structure of the lung. **a**, The attenuation reconstruction shows dense structures such as ribs, spine and the soft tissue well but lacks contrast in the neoprene foam. **b**, The dark-field image is more noisy and less sharp, however, a strong signal from the porous neoprene foam structure is reconstructed. The three cylinders filled with air, sugar, and water can be identified easily.

performance, but some problems, such as the G_0 acceptance, persist and must be addressed in the future. We found that the combination of the large X-ray source spot with the small acceptance of the high aspect ratio G_0 degrades the visibility towards larger fan angles. For now, as a prototype, the performance is sufficiently high in the center and this can be tolerated. A solution could be a structured X-ray source which makes G_0 obsolete by integrating it into the anode, however, currently the X-ray flux is not sufficient for clinical sample sizes, and it would require horizontal instead of vertical grating lines [47].

An important characteristic of the gantry implementation is the stability of the system, and here the focus lies particularly on the vibrations and their origin. We conclude that at the Brilliance iCT gantry, the vibration from the rotating anode (175 Hz) and the electromagnetic distortion of the X-ray source spot (189 Hz) have the strongest impact on the interferometer. Since the frequencies are well sampled at the frame rate of the CT detector and the amplitudes are sufficiently small, so that smearing of fringes is not a major effect, we could not find a negative impact on the system performance. Another important finding is that characteristics of these oscillations are reproducible, which is important for long-time stability, consistency of the results, and is exploited in the data processing. Details about this will be the subject of a future publication. While the low-frequency oscillations – induced by the gantry rotation – are reproducible in phase and amplitude from one scan to the next, the high-frequency variations are only stable in frequency and amplitude, but the oscillation phase is lost between scans.

In order to correct for beam hardening induced dark-field signal, we introduce a correction based on the measured transmission and validate its performance experimentally.

For clinical use, the resolution, and dose of the dark-field CT is an important measure to characterize the proposed system. An experimental evaluation showed that a resolution of up to 2.3 lp/cm at 10% MTF is achieved in the dark-field channel, but varies for the different modalities, i.e., the resolution in the attenuation channel is 4.7 lp/cm at 10% MTF. These results are expected since the modifications of the system and the extended data processing approach come at the cost of spatial resolution loss. Particularly, an implementation of the flying focal spot into dark-field CT could improve this situation, will require more sophisticated data processing and only a deflection in z direction, parallel to the grating lines, is assumed to be feasible without significant drawbacks. Furthermore, advanced processing and reconstruction algorithms such as IBSIR [34] can be applied to increase the spatial resolution by compensating for motion artifacts caused by the sliding window signal extraction.

XI. Conclusion

Considering the hostile environment of a rotating clinical CT gantry into which the Talbot-Lau interferometer is integrated, the identified oscillations are relatively well-behaved. We know from experiments over the last two years that the frequencies and amplitudes are stable over a long time, which allows consistent processing and reconstruction results.

Our current processing scheme allows us to reconstruct at reasonable spatial resolution and free from artifacts, however, further improvements are required, i.e., introduction of the flying focal spot. We could show that the patient dose of a dark-field CT lies within the suggested limits for chest CT examinations. These results demonstrate that clinical dark-field CT is within reach.

Acknowledgment

The authors wish to thank Julia Herzen, Daniela Pfeiffer, Alexander Fingerle, Ernst Rummeny, Peter Noël, Pascal Meyer, Jürgen Mohr, Amanda Pleier, Stefan Löscher, Thomas Reichel, Sven Prevrhal, Ami Altman, and Shlomo Gotman for their help, support, and dedication to launch this complex project.

REFERENCES

[1] S. Schleede et al., "Emphysema diagnosis using X-ray dark-field imaging at a laser-driven compact synchrotron light source," *Proc. Nat. Acad. Sci. USA*, vol. 109, pp. 17880–17885, 2012, doi: 10.1073/pnas.1206684109.

[2] F. G. Meinel et al., "Improved diagnosis of pulmonary emphysema using in vivo dark-field radiography," *Investigative Radiol.*, vol. 49, no. 10, pp. 653–658, Oct. 2014, doi: 10.1097/RLI.0000000000000067.

[3] K. Hellbach et al., "In vivo dark-field radiography for early diagnosis and staging of pulmonary emphysema," *Investigative Radiol.*, vol. 50, no. 7, pp. 430–435, Jul. 2015, doi: 10.1097/RLI.0000000000000147.

[4] K. Hellbach et al., "X-ray dark-field imaging to depict acute lung inflammation in mice," *Sci. Rep.*, vol. 8, no. 1, p. 2096, Dec. 2018, doi: 10.1007/s00134-012-2682-1.

[5] L. Rigon, H.-J. Besch, F. Arfelli, R.-H. Menk, G. Heitner, and H. Plothow-Besch, "A new DEI algorithm capable of investigating sub-pixel structures," *J. Phys. D, Appl. Phys.*, vol. 36, no. 10A, pp. A107–A112, May 2003, doi: 10.1088/0022-3727/36/10A/322.

[6] L. Rigon, A. Astolfo, F. Arfelli, and R.-H. Menk, "Generalized diffraction enhanced imaging: Application to tomography," *Eur. J. Radiol.*, vol. 68, no. 3, pp. S3–S7, Dec. 2008, doi: 10.1016/j.ejrad.2008.04.026.

[7] M. Bech, O. Bunk, T. Donath, R. Feidenhans'l, C. David, and F. Pfeiffer, "Quantitative X-ray dark-field computed tomography," *Phys. Med. Biol.*, vol. 55, pp. 5529–5539, Aug. 2010, doi: 10.1088/0031-9155/55/18/017.

[8] S. K. Lynch et al., "Interpretation of dark-field contrast and particle-size selectivity in grating interferometers," *Appl. Opt.*, vol. 50, pp. 4310–4319, Aug. 2011, doi: 10.1364/AO.50.004310.

[9] M. Strobl, "General solution for quantitative dark-field contrast imaging with grating interferometers," *Sci. Rep.*, vol. 4, p. 7243, Nov. 2014, doi: 10.1038/srep07243.

[10] J. Graetz, A. Balles, R. Hanke, and S. Zabler, "Review and experimental verification of X-ray dark-field signal interpretations with respect to quantitative isotropic and anisotropic dark-field computed tomography," *Phys. Med. Biol.*, vol. 65, no. 23, Nov. 2020, Art. no. 235017, doi: 10.1088/1361-6560/abb7c6.

[11] M. Viermetz et al., "Dark-field computed tomography reaches the human scale," *Proc. Nat. Acad. Sci. USA*, vol. 119, no. 8, Feb. 2022, Art. no. e2118799119, doi: 10.1073/pnas.2118799119.

[12] V. Revol, C. Kottler, R. Kaufmann, U. Straumann, and C. Urban, "Noise analysis of grating-based X-ray differential phase contrast imaging," *Rev. Sci. Instrum.*, vol. 81, no. 7, Jul. 2010, Art. no. 073709, doi: 10.1063/1.3465334.

[13] T. Thuering, P. Modregger, S. Hämmerle, S. Weiss, J. Nüesch, and M. Stampanoni, "Sensitivity in X-ray grating interferometry on compact systems," *AIP Conf. Proc.*, vol. 1466, no. 1, pp. 293–298, Jul. 2012, doi: 10.1063/1.4742307.

[14] L. Birnbacher et al., "Experimental realisation of high-sensitivity laboratory X-ray grating-based phase-contrast computed tomography," *Sci. Rep.*, vol. 6, no. 1, Jul. 2016, Art. no. 24022, doi: 10.1038/srep24022.

[15] S. Bachche et al., "Laboratory-based X-ray phase-imaging scanner using Talbot–Lau interferometer for non-destructive testing," *Sci. Rep.*, vol. 7, no. 1, p. 6711, Dec. 2017, doi: 10.1038/s41598-017-07032-y.

[16] M. Seifert et al., "Talbot–Lau X-ray phase-contrast setup for fast scanning of large samples," *Sci. Rep.*, vol. 9, no. 1, pp. 1–11, Dec. 2019, doi: 10.1038/s41598-018-38030-3.

[17] F. Horn et al., "Implementation of a Talbot-Lau interferometer in a clinical-like c-arm setup: A feasibility study," *Sci. Rep.*, vol. 8, no. 1, p. 2325, Dec. 2018, doi: 10.1038/s41598-018-19482-z.

[18] Z. Wu et al., "Prototype system of noninterferometric phase-contrast computed tomography utilizing medical imaging components," *J. Appl. Phys.*, vol. 129, no. 7, Feb. 2021, Art. no. 074901, doi: 10.1063/5.0031392.

[19] M. Viermetz et al., "Technical design considerations of a human-scale Talbot–Lau interferometer for dark-field CT," *IEEE Trans. Med. Imag.*, early access, Sep. 16, 2022, doi: 10.1109/TMI.2022.3207579.

[20] F. Pfeiffer, T. Weitkamp, O. Bunk, and C. David, "Phase retrieval and differential phase-contrast imaging with low-brilliance X-ray sources," *Nature Phys.*, vol. 2, pp. 258–261, Mar. 2006, doi: 10.1038/nphys265.

[21] T. Weitkamp, C. David, C. Kottler, O. Bunk, and F. Pfeiffer, "Tomography with grating interferometers at low-brilliance sources," *Proc. SPIE*, vol. 6318, Sep. 2006, Art. no. 63180S, doi: 10.1117/12.683851.

[22] T. Donath et al., "Inverse geometry for grating-based X-ray phase-contrast imaging," *J. Appl. Phys.*, vol. 106, no. 5, Sep. 2009, Art. no. 054703, doi: 10.1063/1.3208052.

[23] F. Pfeiffer, C. Kottler, O. Bunk, and C. David, "Hard X-ray phase tomography with low-brilliance sources," *Phys. Rev. Lett.*, vol. 98, no. 10, Mar. 2007, Art. no. 108105, doi: 10.1103/PhysRevLett.98.108105.

[24] F. Pfeiffer et al., "Hard-X-ray dark-field imaging using a grating interferometer," *Nature Mater.*, vol. 7, no. 2, pp. 134–137, 2008, doi: 10.1038/nmat2096.

[25] T. Weitkamp et al., "X-ray phase imaging with a grating interferometer," *Opt. Exp.*, vol. 13, no. 16, p. 6296, 2005, doi: 10.1364/OPEX.13.006296.

[26] T. Weber et al., "Noise in X-ray grating-based phase-contrast imaging," *Med. Phys.*, vol. 38, no. 7, pp. 4133–4140, 2011, doi: 10.1118/1.3592935.

[27] F. J. Koch et al., "Note: Gratings on low absorbing substrates for X-ray phase contrast imaging," *Rev. Sci. Instrum.*, vol. 86, no. 12, Dec. 2015, Art. no. 126114, doi: 10.1063/1.4939055.

[28] N. Gustschin et al., "Quality and parameter control of X-ray absorption gratings by angular X-ray transmission," *Opt. Exp.*, vol. 27, no. 11, May 2019, Art. no. 15943, doi: 10.1364/OE.27.015943.

[29] T. J. Schröter et al., "Large field-of-view tiled grating structures for X-ray phase-contrast imaging," *Rev. Sci. Instrum.*, vol. 88, no. 1, Jan. 2017, Art. no. 015104, doi: 10.1063/1.4973632.

[30] J. Meiser et al., "Increasing the field of view in grating based X-ray phase contrast imaging using stitched gratings," *J. X-Ray Sci. Technol.*, vol. 24, no. 3, pp. 379–388, Jun. 2016, doi: 10.3233/XST-160552.

[31] C. Schmid et al., "Modeling vibrations of a tiled Talbot–Lau interferometer on a clinical CT," *IEEE Trans. Med. Imag.*, early access, Oct. 27, 2022, doi: 10.1109/TMI.2022.3217662.

[32] V. Revol et al., "X-ray interferometer with bent gratings: Towards larger fields of view," *Nucl. Instrum. Methods Phys. Res. A, Accel. Spectrom. Detect. Assoc. Equip.*, vol. 648, pp. S302–S305, Aug. 2011, doi: 10.1016/j.nima.2010.11.040.

[33] R. Behling, *Modern Diagnostic X-Ray Sources: Technology, Manufacturing, Reliability*. Boca Raton, FL, USA: CRC Press, 2021, doi: 10.1201/9781003095408.

[34] M. von Teuffenbach et al., "Grating-based phase-contrast and dark-field computed tomography: A single-shot method," *Sci. Rep.*, vol. 7, p. 7476, Aug. 2017, doi: 10.1038/s41598-017-06729-4.

[35] D. Devitt, "Radial air bearings help CT scanners see into your heart," *Des. World Mag.*, pp. 62–64, Dec. 2009. [Online]. Available: https://www.designworldonline.com/radial-air-bearings-help-ct-scanners-see-into-your-heart/

[36] J. Hsieh, *Computed Tomography: Principles, Design, Artifacts, and Recent Advances*, 3rd ed. Bellingham, WA, USA: SPIE, 2015, doi: 10.1117/3.2197756.

[37] W. Yashiro, P. Vagovic, and A. Momose, "Effect of beam hardening on a visibility-contrast image obtained by X-ray grating interferometry," *Opt. Exp.*, vol. 23, no. 18, pp. 23462–23471, 2015, doi: 10.1364/OE.23.023462.

[38] F. D. Marco et al., "X-ray dark-field signal reduction due to hardening of the visibility spectrum," 2020, *arXiv:2011.03542*, doi: 10.48550/arXiv.2011.03542.

[39] G. Pelzer et al., "A beam hardening and dispersion correction for X-ray dark-field radiography," *Med. Phys.*, vol. 43, pp. 2774–2779, May 2016, doi: 10.1118/1.4948671.

[40] J. Wang and D. Fleischmann, "Improving spatial resolution at CT: Development, benefits, and pitfalls," *Radiology*, vol. 289, no. 1, pp. 261–262, Oct. 2018, doi: 10.1148/radiol.2018181156.

[41] M. Kachelriess, M. Knaup, C. Penssel, and W. A. Kalender, "Flying focal spot (FFS) in cone-beam CT," *IEEE Trans. Nucl. Sci.*, vol. 53, no. 3, pp. 1238–1247, Jun. 2006, doi: 10.1109/TNS.2006.874076.

[42] I. Zanette et al., "Quantitative phase and absorption tomography with an X-ray grating interferometer and synchrotron radiation," *Phys. Status Solidi A*, vol. 208, no. 11, pp. 2526–2532, Nov. 2011, doi: 10.1002/pssa.201184276.

[43] J. Hsieh, "Adaptive streak artifact reduction in computed tomography resulting from excessive X-ray photon noise," *Med. Phys.*, vol. 25, no. 11, pp. 2139–2147, 1998, doi: 10.1118/1.598410.

[44] X. Ji, Y. Ge, R. Zhang, K. Li, and G.-H. Chen, "Studies of signal estimation bias in grating-based X-ray multicontrast imaging," *Med. Phys.*, vol. 44, no. 6, pp. 2453–2465, Jun. 2017, doi: 10.1002/mp.12235.

[45] (2016). *American Association of Physicists in Medicine, Adult Routine Chest CT Protocols*. [Online]. Available: https://www.aapm.org/pubs/CTProtocols/

[46] *Evaluation and Routine Testing in Medical Imaging Departments Constancy Tests*, British Standard BS EN 61223-2-6:2007, 2006. [Online]. Available: https://webstore.ansi.org/Standards/BSI/BSEN612232007

[47] G. Zan et al., "High-resolution multicontrast tomography with an X-ray microarray anode-structured target source," *Proc. Nat. Acad. Sci. USA*, vol. 118, no. 25, Jun. 2021, Art. no. e2103126118, doi: 10.1073/pnas.2103126118.